

# Acoustic and dynamic mechanical properties of a polyurethane rubber

Peter H. Mott<sup>a)</sup> and C. Michael Roland

*Chemistry Division, Naval Research Laboratory, Washington, DC 20375-5320*

Robert D. Corsaro

*Acoustics Division, Naval Research Laboratory, Washington, DC 20375-5320*

(Received 13 June 2001; accepted for publication 17 January 2002)

Acoustical and dynamic mechanical measurements were carried out on a commercial polyurethane rubber, DeSoto PR1547. The sound speed and attenuation were measured over the range from 12.5 to 75 kHz and 3.9 to 33.6 °C. Shear modulus was measured from  $10^{-4}$  to 2 Hz and –36 to 34 °C. The peak heights of the shear loss tangent varied with temperature, demonstrating thermorheological complexity. At higher temperatures, time–temperature superpositioning could be applied, with the shift factors following the Williams–Landel–Ferry equation. From the combined acoustical and mechanical measurements, values for the dynamic bulk modulus were determined. Moreover, superposition of the bulk modulus data was achieved using the shift factors determined from the dynamic mechanical shear measurements. Finally, this work illustrates the capability and the working rules of acoustical measurements in a small tank. [DOI: 10.1121/1.1459465]

PACS numbers: 43.58.Dj, 43.35.Mr [SLE]

## I. INTRODUCTION

To understand the relaxation processes of polymers above the glass transition temperature  $T_g$ , it is necessary to determine how molecular motions, kinematically coupled to produce both bulk (volume) and shear relaxations, are governed by the structure of the chain molecules. Bulk viscoelastic behavior is fundamentally different from the shear properties. Bulk relaxations reflect very local motions of the polymer molecules, and are thus insensitive to long-range structural features, such as entanglements and crosslinks.<sup>1</sup> On the other hand, at low frequency and/or high temperature, the terminal dynamics associated with shear flow involve much longer lengths of the chain, with entanglements having a pronounced effect.

Direct measurement of the dynamic bulk modulus at frequencies above 1 kHz is difficult. Early measurements were made by Philippoff and Brodnyan<sup>2</sup> using a piston–cylinder arrangement with mercury as the confining fluid. This determination was limited to frequencies below 5 Hz. Marvin and collaborators<sup>3,4</sup> measured the dynamic bulk modulus over a wider frequency range for a soft elastomer, constructing master curves encompassing a broad range of reduced frequency. Dubbelday and co-workers<sup>5,6</sup> employed this data reduction technique to determine bulk modulus shift factors for four different elastomers; unfortunately, PR1541 polyurethane was not evaluated. More recently, Holownia and James<sup>7</sup> developed a differential pressure technique and Willis *et al.*<sup>8,9</sup> employed interferometry to obtain dynamic bulk modulus data. All these direct methods are limited to relatively low frequencies, usually less than 5 kHz.

Because of the practical difficulties with the above techniques, indirect measurements of the bulk modulus are sometimes employed. For example, Litovitz and co-workers<sup>10</sup> determined the dynamic bulk compliance by subtracting the

shear from the longitudinal complex compliance, both measured ultrasonically, for low molecular weight glass-forming liquids. DiMeglio and Wang<sup>11</sup> have introduced a variational algorithm to find dynamic elastic moduli from acoustical measurements of butyl rubbers. Another interesting technique, introduced by Piquette,<sup>12</sup> used acoustic scattering to obtain the bulk and shear moduli of rubbery spheres.

In this article we report the sound speed  $c$  and attenuation coefficient  $\alpha$  for a low-loss polyurethane elastomer. The measurements, performed in a small laboratory tank, were carried out over the frequency range from 12.5 to 75 kHz at temperatures from 3.9 to 33.6 °C. We also obtained dynamic mechanical shear data on the same material, at lower frequencies over a broader temperature range. When combined, these data provide an estimate of the dynamic bulk modulus.

Also described herein are some working rules for using large-area transducers in small tanks. These were developed two decades ago, at a time when facilities were under development to evaluate the acoustic properties of new materials for underwater applications. These working rules were derived from practical experience and have not been previously documented.

## II. EXPERIMENT

### A. Sample preparation and shear measurements

The proper sample thickness is governed by many factors. For acoustical measurements, increasing the sample thickness provides higher measurement resolution. However, in very thick samples, internal reflections and waveguide behavior can decrease the accuracy and measurement window available (discussed shortly). Other practical considerations include material cost, difficulty of fabrication, and the increased likelihood that thick samples will include defects.

For the present study we selected a thickness of 52 mm. The two-part amber PR1547 polyurethane (PRC-DeSoto International) was mixed according to the manufacturer's pro-

<sup>a)</sup>Electronic mail: phm@xbt.nrl.navy.mil

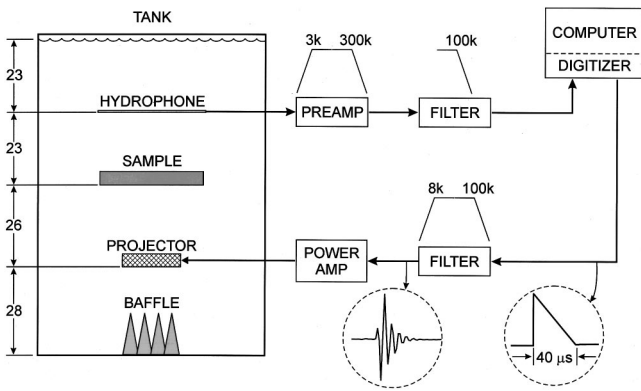


FIG. 1. Schematic of the sound speed experimental apparatus. The vertical placements within the tank—baffle, projector, sample, hydrophone, and water surface—are given in cm. The sample was  $35 \times 35 \times 5.2 \text{ cm}^3$ . See text for further discussion.

cedure. To reduce the likelihood of entrapping air bubbles, the specimen was cast as a four-layer composite, with each layer added in turn, degassed, and cured overnight at  $80^\circ\text{C}$  before adding the next layer. Samples prepared for dynamic mechanical measurements were cut from a 4.5-mm-thick sheet, cured similarly. The Shore A durometer of the material was 80, consistent with the manufacturer's specifications.

Characterization of the isothermal shear dynamic properties of the material was performed using a Bohlin VOR rheometer with parallel plate geometry. A cylindrical sample, 12 mm diameter  $\times$  4.5 mm height, was glued to the plates with cyanoacrylate adhesive. The applied torque was continually adjusted over the frequency scan to maintain a 28 kPa shear stress. The maximum torsional strain did not exceed 0.6%, which is well within the limits of linearity. To prevent debonding during the measurements, the sample was subjected to a small compressive load (5.2 kPa). Typically, the shear moduli are repeatable to within 10%.

## B. Sound speed apparatus

A schematic of the sound speed apparatus and measurement system is given in Fig. 1. The tank was cylindrical ( $0.724 \text{ m diameter} \times 1.01 \text{ m tall}$ ), and its acoustical characteristics and use for reflectivity measurements have been described previously.<sup>13</sup> The temperature of the ion-exchanged water was controlled by a Neslab refrigerated recirculator, which was allowed to equilibrate overnight.

The projector and hydrophone were both directive large area devices. The sound projector was the F33 standard<sup>14</sup> (from Underwater Sound Reference Division, Naval Undersea Warfare Center). The hydrophone was  $30 \times 30 \text{ cm}^2$ , constructed from poly(vinylidene fluoride) (PVDF) sheets (Kynar film, from Measurement Specialties, Inc.) with silver ink electrodes. This hydrophone was fabricated from three layers of PVDF,<sup>15</sup> but is operationally equivalent to a four-layer design arranged as a dual differential bimorph. Each bimorph is of a conventional type used to suppress the signal generated by bending. Pairing these bimorphs places electrical ground planes on the exterior surfaces, thus providing electrical shielding. As usual for PVDF hydrophones,<sup>16</sup> a thin aluminum shim layer is included to suppress lateral modes.

Large-area thin-film PVDF transducers have been in routine use in various laboratories for many years, both as projectors and hydrophones. Because of their inherent area averaging response and their favorable acoustic transparency, they have found use in material property and structural acoustical studies. Two of the largest such arrays presently in use are the  $71 \times 71 \text{ cm}^2$  array of Morse,<sup>17</sup> and the  $285 \times 76 \text{ cm}^2$  array at NRL. Such hydrophones typically operate over a very broad frequency bandwidth, often extending to 500 kHz. Their frequency response is reasonably flat over most of their operating range, but calibration is required to identify select frequency regions which may contain geometry dependent features. They are typically stable and relatively temperature and pressure independent. Their chief drawback is their rather low sensitivity, typically near  $-215 \text{ dB re: } 1 \mu\text{Pa}$ . This restricts their use to relatively high signal levels.

## C. Sample placement

The locations of the projector, hydrophone, and sample were chosen to provide a maximum echo-free time window within the height constraint of the tank. The sound projector is positioned about one-quarter of the way from the tank bottom; the hydrophone was similarly located about one-quarter of the way from the top water surface (see Fig. 1). The sample, placed at the midpoint, could be removed or inserted without disturbing the position of the hydrophone.

For the above geometry, the first arriving interfering echoes have paths corresponding to projector-bottom-projector, sample-projector-sample, hydrophone-sample-hydrophone, and hydrophone-surface-hydrophone. All of these have path lengths nominally 42 cm greater than that of the direct signal (including the sample thickness). Hence these interfering echoes arrive approximately 250  $\mu\text{s}$  after the direct signal.

If the measurement time window is small, it can be the determining factor governing the lowest frequency at which reliable data can be obtained. This low-frequency limit is set by the nominal working requirement that (without special processing) the measurement time window be sufficient to include at least 1.5 waves plus the time required for one round-trip within the sample. In practice, due to ring-down transients of the projector, it is desirable to have a measurement time window that is long enough to include the observable end of the signal of interest. For the impulse-type source signals used here, this requirement becomes nominally the duration of three waves at the lowest frequency of interest.

For the above case, the available 250- $\mu\text{s}$  time window would therefore allow measurements to frequencies as low as 12 kHz using the three-wave guidance.

## D. Sample size and edge diffraction

There is a considerable body of theoretical literature related to the influence of a lateral finite sample size on reflectivity and insertion loss measurements.<sup>18,19</sup> A summary of

established practice is contained in a recent report by Piquette.<sup>20</sup> These treatments typically concentrate on the interference signal arriving from the edge-diffracted wave, and use idealized cases such as point or plane-wave source and receiver. While applicable in the standard test arrangements used in underwater evaluation facilities, they provide only coarse guidance in cases of closely spaced finite-size transducer elements.

Simple point transducers cannot be used at low frequencies in the current (relatively small) facility. We briefly consider this case of point transducers as a starting point due to their common use in small tanks at high frequencies, and occasionally their improper use in such tanks at low frequencies. The lowest frequency that can be used with a test article in transmission is typically limited by the arrival of an edge-diffracted wave. For the case of point source and point receiver, the arrival time of this wave can be calculated from the geometry. For the separation distances and sample size used here, the earliest edge-diffracted wave would arrive 75  $\mu\text{s}$  after the direct wave. (Due to the square sample geometry, additional edge-diffracted components would arrive with progressively lower amplitude for up to 140  $\mu\text{s}$  after the direct wave.) Using the above three-wave rule for the available time window gives a lowest usable frequency of only 40 kHz. Even extending to the 1.5-wave rule allows measurements only as low as 20 kHz.

Since the time window of the measurement will therefore include edge-diffracted waves, it becomes important to ensure that the magnitude of their contribution is negligible. This is encouraged by using large-area transducers, which suppress off-axis contributions due to their directivity. Additionally, since the magnitude of a diffracted wave is related to the impedance mismatch, it is helpful to use test samples having a specific acoustic impedance not much different from that of water.

The improvement attainable with large-area transducers is predictable, but somewhat complicated. It involves initially calculating the signal received at the surface of the hydrophone. This double integral can be performed in a more computationally efficient manner by approximating the actuator and sensor areas as disks, such that one can use the variable transform approach of Archer-Hall and Gree.<sup>21</sup> The approach finds that the pressure at any field point from a disk radiator,  $P_1$ , can then be expressed by the single integral

$$P_1 = P_\sigma \left\{ \begin{aligned} & \left[ \begin{array}{ll} 0, & b > a \\ \frac{1}{2}, & b = a \\ 1, & b < a \end{array} \right] e^{-ikz} \\ & + \frac{1}{\pi} \int_0^\pi e^{-iks} \left( \frac{ab \cos \theta - a^2}{a^2 + b^2 - 2ab \cos \theta} \right) d\theta \end{aligned} \right\}, \quad (1)$$

where  $P_\sigma$  is the pressure at the surface,  $a$  is the radius of the projector,  $b$  and  $z$  are distances between the field point and the disk radiator along the disk radial and normal directions, respectively,  $k$  is the wave number, and  $\theta$  is the azimuth angle. The quantity  $s$  is defined as

$$s \equiv \sqrt{a^2 + b^2 + z^2 - 2ab \cos \theta}. \quad (2)$$

The pressure sensor output is then found by integrating this field over the area of the sensor,

$$\bar{P} = \frac{2}{a^2} \int_0^a b P_1 db. \quad (3)$$

For transmission estimates, the process is then repeated using the appropriate sample aperture, as developed by N. Yen.<sup>22</sup> (For reflectivity estimates, the approach is similar but an image method is used.)

The above procedure is too complicated for routine laboratory use. Instead some simple “rules-of-thumb” have been developed by experimentalists when collecting data with such finite-size transducers. These were arrived at from direct observations of laboratory data, on a wide range of materials. Such tests were conducted in various tank facilities, including the facilities located at the Naval Research Laboratory (Washington, DC), the Underwater Sound Reference Division (Orlando, FL), and the Naval Surface Warfare Center (Crane, IN).

These working rules are intended only as guidance in initial selection of sample size, and certainly do not guarantee valid data over the given frequency range. They are as follows, where the size referred to is the smallest (lateral) width, and  $\lambda$  is the wavelength of sound in water. For insertion loss measurements on flat samples at normal sound incidence, typically the sample should be at least  $4\lambda$  in width. If the impedance of the sample is not too different from that of water and the loss is not very high, then the amplitude of the edge-diffracted wave will be small relative to the transmitted wave. In combination with directional hydrophones, reliable sound speed data can then be obtained for sample sizes as small as  $3\lambda$ .

Based on the above, the current  $35 \times 35 \text{ cm}^2$  sample size and directive transducers should permit sound speed data to frequencies nominally as low as 12.7 kHz. These recommendations of minimum sample size are provided as rough guides, and only apply to the usual test arrangements, and data collection and analysis procedures. They do not apply to more computationally extensive techniques. They are supported by the observation that data accuracy on known samples typically appears noticeably degraded as these limits are exceeded.

## E. Data sampling

The laboratory data acquisition system available was a Powerlab (ADI Instruments, Inc.) used in connection with a desktop computer (PowerMac G3). This system has a maximum sampling rate of only 200 kHz, and this rate is available only in the single-channel mode. This permits sampling at 2.5 points per cycle at 80 kHz, the highest signal frequency of interest in this study. While the sampling theorem indicates that this rate is entirely satisfactory, some care is required when sampling this close to the Nyquist limit.

The source signal is a  $40\mu\text{s}$  sawtooth pulse, generated by the digitizer. The rapid rise time of this signal provided a reasonably uniform excitation over the frequency band of interest; the slow return ramp reduced turn-off transients.

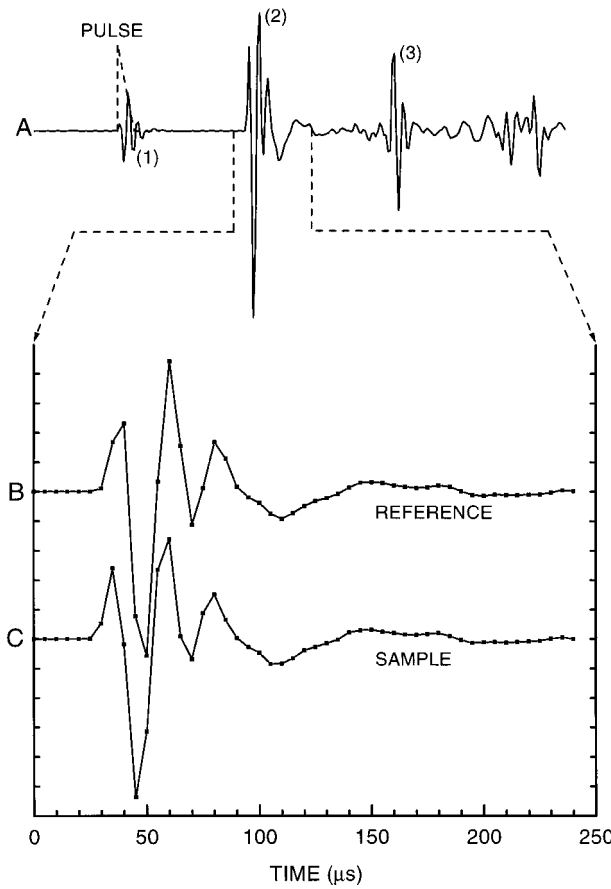


FIG. 2. Time records for a representative sound speed measurement. Trace A is the complete record, with the first pulse (1) coincident with saw-tooth excitation pulse (indicated by the dashed line). The next pulse (2) is the received direct signal, which is shown on an expanded scale as traces B (with sample in place) and C (with sample removed). The following pulse (3) is the reflection from the upper water surface.

This pulse then passed through an 8–100-kHz band-pass filter, which removed out-of-band signals, including particularly low-frequency off-sets. This filtered signal was amplified and applied to the projector. The hydrophone output was directed through a differential preamplifier and a 12-dB/oct 100-kHz low-pass filter.

Each signal is averaged over 128 pulses by the acquisition system. Low-pass filtering also occurred in other system elements (preamplifier, projector, etc.) and was sufficient to prevent aliasing at the sample rate used. Since the source signal is synchronized to the digitizing or sampling rate, an additional timing reference channel is not needed.

#### F. Sound speed data analysis

A series of representative time records for a single measurement is shown in Fig. 2. Trace A is the complete record with the sample in place. The dashed line represents the 40- $\mu$ s sawtooth excitation pulse. The first received pulse, coincident with the excitation, is electrically induced. The second pulse is the sound transmitted through the sample. The third pulse is the reflection from the upper surface of the water (identified by disturbing the surface), and subsequent pulses are reflections from other surfaces. Traces B and C compare the second pulse, with the sample and without (la-

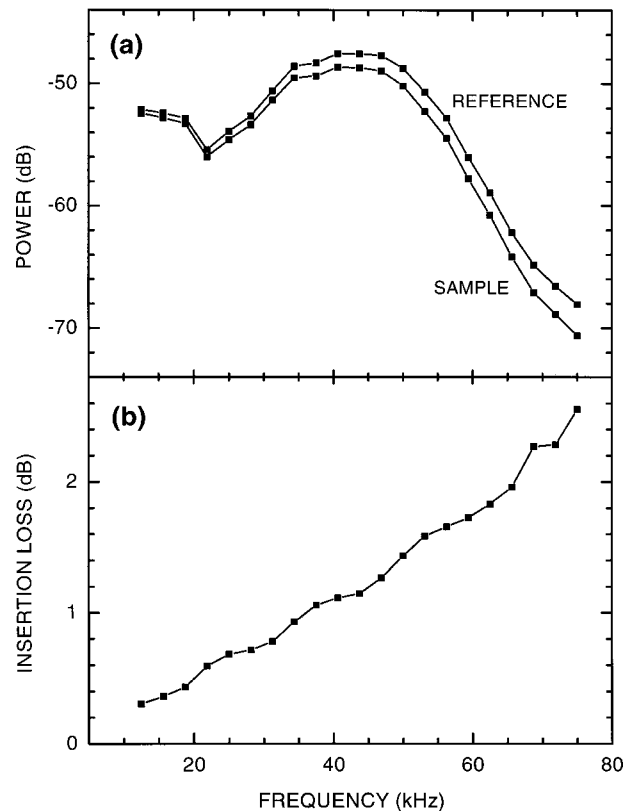


FIG. 3. (a) Fourier transform (power spectrum) of traces B and C of Fig. 2. (b) Insertion loss, defined as the difference between the two curves above.

beled “reference”); the difference between the two signals is subtle, but accurately resolvable by the instrumentation used.

The Fourier transform of traces B and C are shown in Fig. 3(a). The time window of the transform was made as wide as possible, without including extraneous reflections. The frequency response is governed by the signal, the characteristics of the transducers, and the filters.

The difference in the magnitudes of these spectra in decibels is the insertion loss [Fig. 3(b)], or when expressed as a simple ratio is the transmissibility. This was used to evaluate the attenuation coefficient  $\alpha$ . In the usual procedure for evaluating  $\alpha$  from transmissibility, the reflectivity is also measured, and the attenuation coefficient is then obtained only after correcting the transmissibility for the loss due to reflections. In this case, however, the measured sound speed, density, and attenuation indicate a value for the specific acoustic impedance that is reasonably close to that of water. The resulting reflection loss is then a negligible component in the calculation.

The speed of sound in this sample is calculated from the phase difference between these two spectra using

$$c = \frac{1}{1/c_w + \phi/360ft}, \quad (4)$$

where  $\phi$  is the phase difference, in degrees, between the reference and the sample signals,  $f$  is the frequency in Hz, and  $t$  is the sample thickness. The sound speed in water  $c_w$  is given by<sup>23</sup>

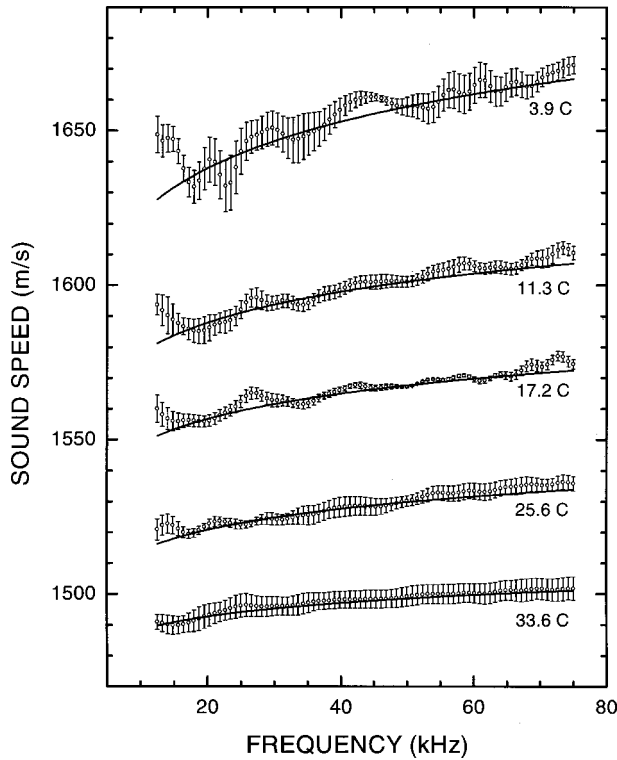


FIG. 4. Sound speed (average of four measurements) determined from phase difference [Eq. (4)]; the error bars represent one standard deviation. The solid lines are the fit from the attenuation data (Fig. 5) and the Kramers–Kronig relation [Eq. (6)].

$$c_w = 1402.7 + 4.88T - 0.0482T^2 + 1.35 \times 10^{-4}T^3 \text{ (in m/s)}, \quad (5)$$

where  $T$  is the temperature in Celsius.

### III. RESULTS AND DISCUSSION

#### A. Sound speed and attenuation

Figure 4 shows the measured sound speed. The data points represent the average of the individual measurements (four per temperature), and the error bars are one standard deviation. (The smooth curves are not fits to the data, as described below.) As the temperature increases, both the magnitude and the frequency dependence of  $c$  are observed to decrease.

Sound attenuation values are shown in Fig. 5, where again the points are averages, and the error bars represent one standard deviation. The lines are linear least-squares fits to the data, constrained to pass through the origin. As the temperature increases, the slope of the frequency-dependence decreases. Table I summarizes these results; the uncertainty represents one standard deviation.

The internal consistency of these results can be verified from the Kramers–Kronig relations,<sup>24,25</sup> which, for small dispersion, reduces to the following expression for the attenuation coefficient:<sup>26</sup>

$$\alpha(f) = \frac{\pi^2 f}{c^2} \frac{dc}{df}. \quad (6)$$

Taking the ratio  $\alpha/f$  to be a constant (namely  $A$ , the slope of straight lines of Fig. 5), Eq. (6) is integrated to yield

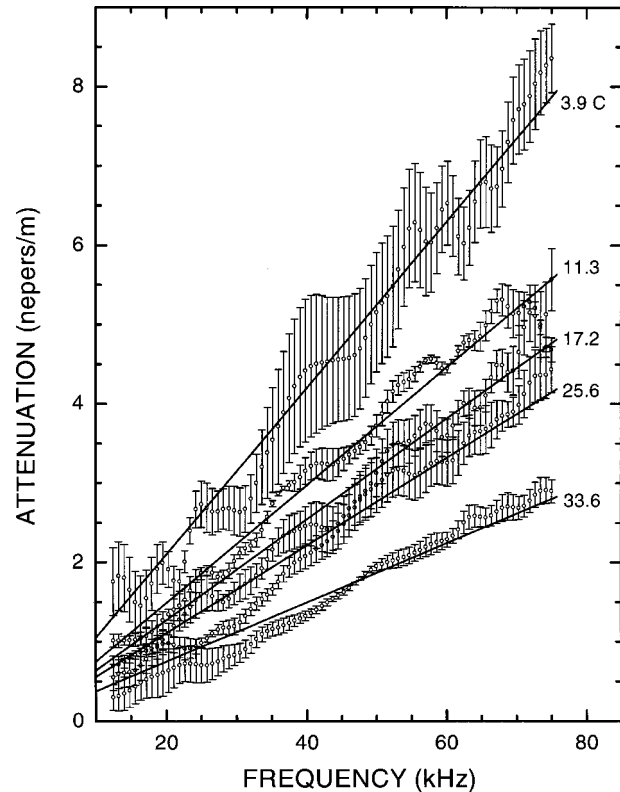


FIG. 5. Sound attenuation at the indicated temperatures. Circles represent the average of four trials, and the error bars indicate one standard deviation. The solid lines are linear least square fits constrained to pass through the origin.

$$c(f) = \frac{c_0}{1 - (Ac_0/\pi^2)\ln(f/f_0)}, \quad (7)$$

where  $c_0$  is the sound speed at an arbitrary reference frequency,  $f_0 = 43$  kHz. The values of  $c_0$ , along with the uncertainty, were derived from a straight line fit through the data displayed in Fig. 4, and are listed in Table I. The resulting Kramers–Kronig curves are drawn in Fig. 4, and the agreement with the data is seen to be excellent. This agreement provides support for the sample size “rules-of-thumb” discussed above.

#### B. Shear modulus

The complex shear modulus,  $G^*$ , and loss tangent ( $\tan \delta_G \equiv G''/G'$ , the ratio of the loss to the storage moduli) were obtained over the temperature range of  $-36^\circ\text{C}$  to  $34^\circ\text{C}$ , at frequencies from  $10^{-4}$  to  $2$  Hz with the Bohlin VOR rheometer. The results are shown in Fig. 6.

TABLE I. Sound speed parameters.

Temperature (°C)	Attenuation slope ( $\times 10^{-6}$ nepers/(m/s))	Sound speed <sup>a</sup> (m/s)
3.9	$104.93 \pm 0.68$	$1654.5 \pm 1.61$
11.3	$74.30 \pm 0.51$	$1598.9 \pm 0.76$
17.2	$63.55 \pm 0.52$	$1565.7 \pm 0.61$
25.6	$55.27 \pm 0.53$	$1528.3 \pm 0.31$
33.6	$37.34 \pm 0.35$	$1497.5 \pm 0.42$

<sup>a</sup>From a linear fit to Fig. 4, at 43.0 kHz.

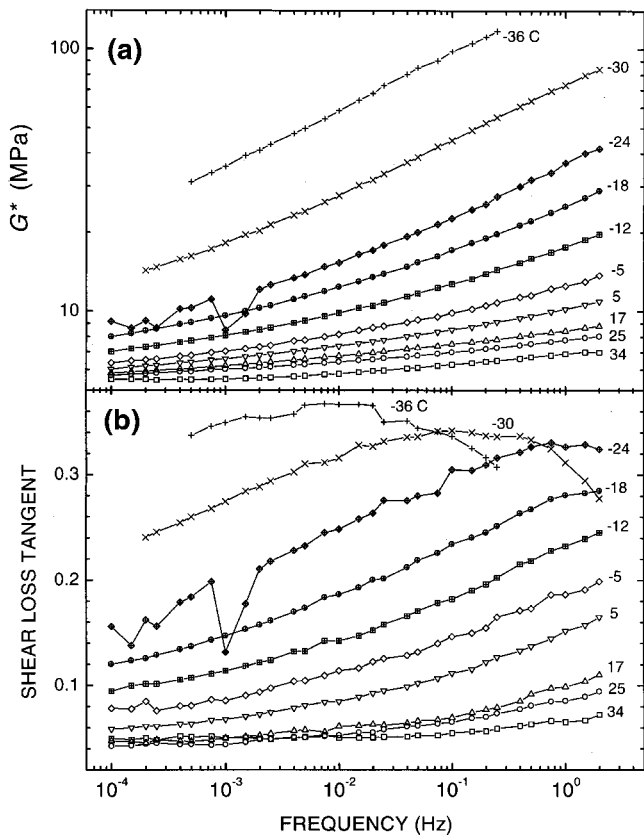


FIG. 6. The dynamic shear modulus (a) and tangent of the phase angle (b), at the indicated temperatures.

Temperature–frequency shift factors,  $a_T$ , were determined by superposition of the loss tangent data. These same shift factors were used, along with small vertical shifting, to construct the master curve for the dynamic modulus shown in Fig. 7.

Deviations from the time–temperature superposition principle are evident in the loss tangent data at higher frequencies. These deviations become evident in the softening (glass–rubber transition) zone of the viscoelastic spectrum, due to intrusion of the local segmental relation, which has a different temperature dependence than the chain modes probed at lower frequency. The result is a systematic increase in the height of the loss tangent as temperature decreases. Such thermorheological complexity has been seen previously in a variety of polymers, including 1,4-polyisoprene,<sup>27</sup> polystyrene,<sup>28</sup> poly(vinyl acetate),<sup>29</sup> polypropylene glycol,<sup>30</sup> poly(phenylmethyl siloxane),<sup>31</sup> polybutadiene,<sup>32</sup> polyisobutylene,<sup>33</sup> and atactic polypropylene.<sup>34,35</sup> The breakdown of time–temperature superposition is a consequence of both local segmental motion and the polymeric chain modes contributing to the dynamics in this region of the spectrum.

For reduced frequencies below the transition zone (i.e., temperatures higher than the transition zone), the time–temperature superposition principle provides a good description of the data. In this region, the shift factors were fit to the Williams–Landel–Ferry (WLF) equation,<sup>36</sup>

$$\log a_T = \frac{-C_1(T-T_0)}{C_2+T-T_0}. \quad (8)$$

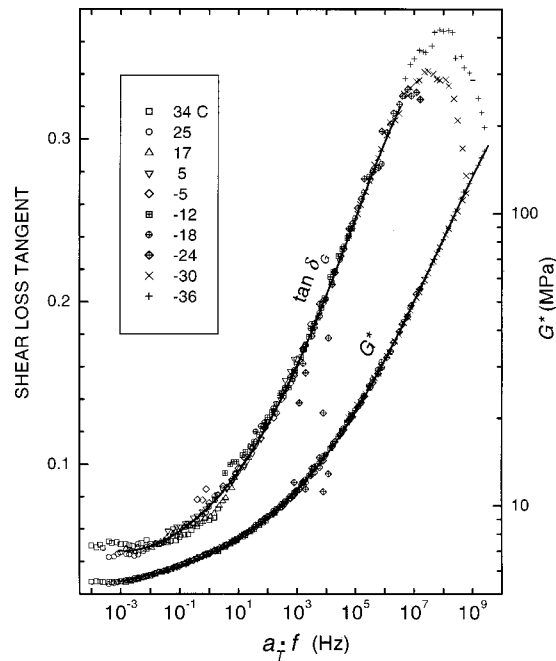


FIG. 7. Master curves of the complex shear modulus and loss tangent. The solid lines are fifth-order polynomial fits. The breakdown in time–temperature superposition is evident in the loss tangent at high frequencies.

The obtained parameters,  $C_1$  and  $C_2$ , the reference temperature  $T_0$ , and previously reported WLF parameters for PR1547 polyurethane<sup>37</sup> (converted to the same reference temperature) are listed in Table II. Figure 8 displays  $\log a_T$  as a function of temperature. The present shift factors agree with the earlier results at higher temperatures, but deviate below about 5 °C. This is not unexpected, since the previous measurements only extended down to –5 °C. As the comparison in Fig. 8 makes clear, extrapolation of shift factors to temperatures beyond the measured range can entail large error.

### C. Bulk modulus

The frequency-dependent bulk modulus,  $B^*$ , can be found from the sound speed, attenuation, and dynamic shear modulus, using the relations<sup>38</sup>

$$M^* \approx M' = \rho c^2, \quad (9)$$

$$\tan \delta_M = \frac{\alpha c}{\pi f}, \quad (10)$$

and

$$B^* = M^* - \frac{4}{3}G^*, \quad (11)$$

where  $\rho$  is the density,  $M^*$  is the complex longitudinal modulus, and  $\tan \delta_M (=M''/M')$  is analogous to the shear loss tangent. The temperature-dependent density was deter-

TABLE II. Williams–Landel–Ferry (WLF) equation parameters.

	This study	Reference 37
$C_1$	7.391	4.2241
$C_2$ (C)	119.6	72.6
$T_0$ (C)	34	34

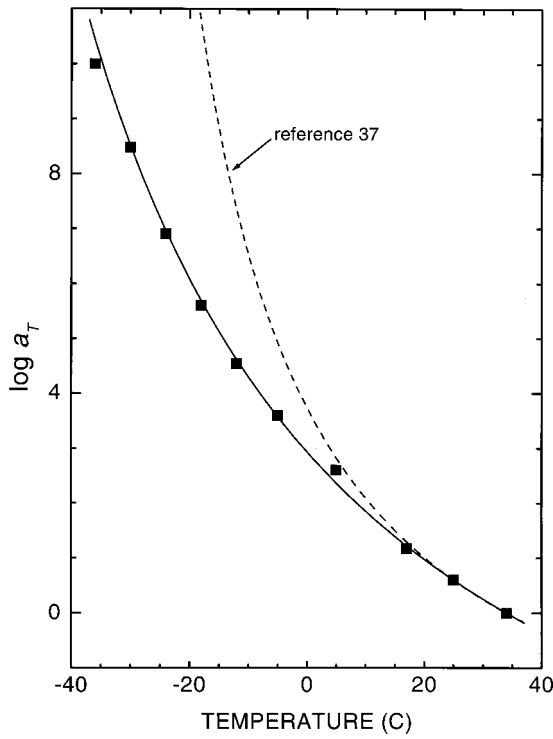


FIG. 8. Time–temperature shift factors ( $\log a_T$ ), corresponding to the master curves in Fig. 7. Also included as the dashed line is the WLF equation fit to this same material reported by Capps (Ref. 37).

mined by combining the room temperature value (manufacturer specifications:  $1050 \text{ kg/m}^3$ ) with the thermal expansion coefficient. The latter was found from the variation of the sample gap during the shear experiments,  $1.28 \pm 0.05 \times 10^{-3} \text{ }^\circ\text{C}^{-1}$ , over for the temperature range  $-36$  to  $34 \text{ }^\circ\text{C}$ . The frequency-dependent values of  $M'$  were calculated from the sound speed data shown in Fig. 4, with  $\tan \delta_M$  deduced from the attenuation measurements shown in Fig. 5. To determine the storage and loss components of the dynamic bulk modulus [Eq. (11)], the corresponding values of  $G$  were taken from polynomial fits to the shear master curves, as shown in Fig. 7. The calculated values of the bulk storage,  $B'$ , and loss,  $B''$ , moduli are shown in Fig. 9. At the lowest temperature,  $3.9 \text{ }^\circ\text{C}$ , the data are less reliable due to the breakdown in time–temperature superposition noted in Fig. 7. The magnitudes of the shear moduli are approximately 1% of the bulk moduli, as expected for an incompressible material. However, the shear modulus has a stronger frequency dependence, giving rise to the slopes of the lines in Fig. 9.

As suggested by previous work,<sup>1,3,4</sup> the horizontal shift factors for the dynamic shear modulus were used to generate master curves for  $\tan \delta_B (= B''/B')$  and the complex bulk modulus. These results are shown in Fig. 10. The vertical shifting used to superimpose  $B^*$  increased linearly from 0.875 to unity over the temperature interval. Again, due to the breakdown in time–temperature superpositioning, the data are less reliable at the higher reduced frequencies (corresponding to the lowest measurement temperature,  $3.9 \text{ }^\circ\text{C}$ ).

In general, published data on bulk modulus shift factors are limited.<sup>3–6</sup> The near equivalence of the shift factors for bulk and shear deformations suggests that similar molecular mechanisms govern both. On the other hand, thermorheo-

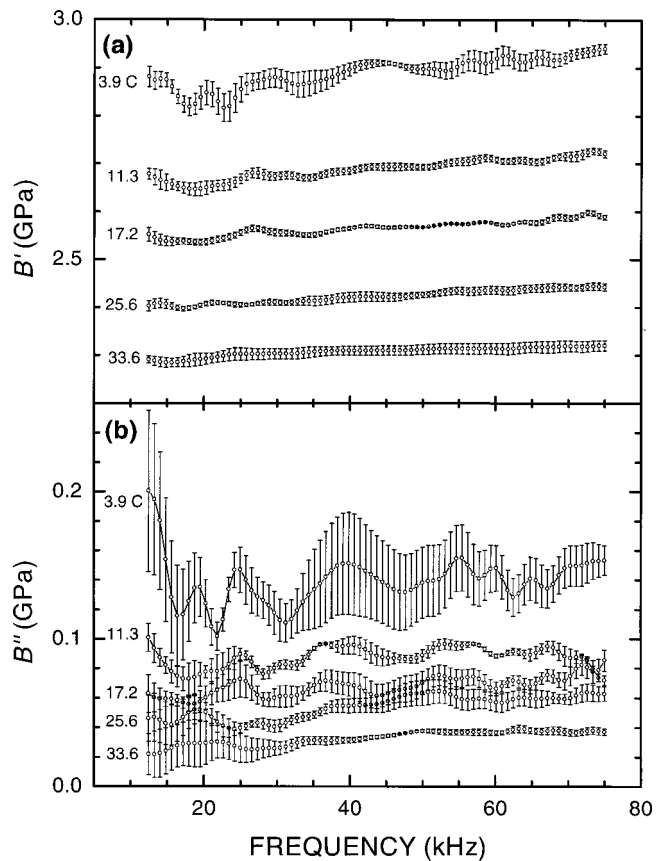


FIG. 9. Calculated bulk storage (a) and loss (b) moduli, at the indicated temperatures, found by combining the sound speed (Fig. 4), attenuation (Fig. 5), and the shear master curves (Fig. 7), using Eqs. (9)–(11). The points are the averages of four trials, and the error bars mark one standard deviation.

logical complexity, demonstrated by the varying  $\tan \delta_G$  peak heights in Fig. 7, indicates that the local segmental motions and polymeric chain modes have a different temperature dependence. This implies that the chain modes, not the local segmental motions, underlie relaxation of the bulk modulus, at least over the range of experimental temperatures and frequencies probed herein. These differences in temperature dependence are not evident over a relatively narrow frequency range, such as in Fig. 10.

Comparisons between the time scales of relaxation for different processes have been carried out for a few polymers.<sup>39–43</sup> Much of this work is focused on the volumetric effects of physical aging below  $T_g$ , where the material is not at its equilibrium density. Above  $T_g$ , Bero and Plazek<sup>39</sup> found that the time–temperature shift factors agree between volume and creep for both constant cooling rate and constant temperature jump experiments. Thus, the agreement of the dynamic bulk and shear moduli shift factors is in accord with related experimental results.

#### IV. CONCLUSIONS

Sound speed and attenuation were measured for a commercial polyurethane, DeSoto PR1547, over the range from 12.5 to 75 kHz and  $3.9$  to  $33.6 \text{ }^\circ\text{C}$ ; the complex shear moduli were measured from  $10^{-4}$  to 2 Hz and  $-36$  to  $34 \text{ }^\circ\text{C}$ . The accuracy of the former was affirmed from consistency with

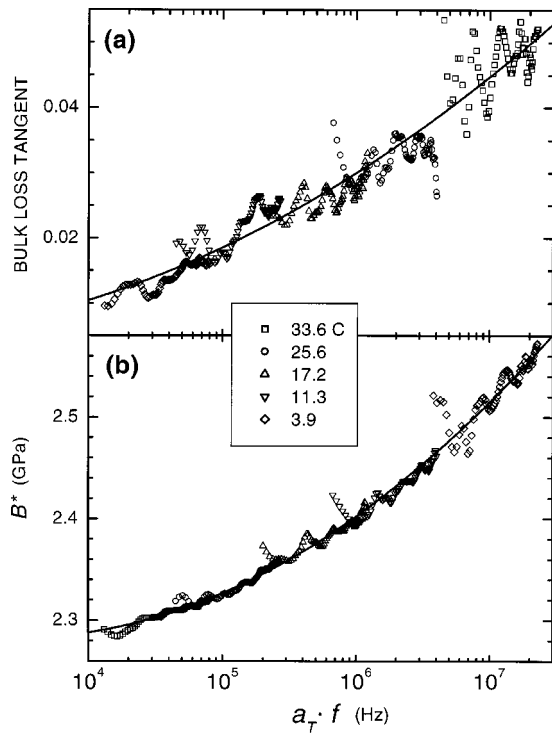


FIG. 10. Master curves of the bulk lost tangent (a) and complex bulk modulus (b) (data adapted from Fig. 9). The error bars are not shown for clarity. The horizontal shift factors  $a_T$  for the loss tangent were taken from the shear modulus, Fig. 8.

the Kramers–Kronig relation. By combining the sound speed and dynamic mechanical data, master curves were constructed for the complex bulk moduli. Although there was apparent agreement between the shift factors for bulk and shear deformation, this is probably due to the narrow range of measurement frequencies. This work illustrates the capability and some of the working rules associated with acoustical measurements in a small tank, as well as the use of such data to deduce material properties.

## ACKNOWLEDGMENTS

We thank Dr. P. G. Santangelo for his insights and assistance with the dynamic mechanical measurements, and Dr. K. L. Ngai, Dr. G. B. McKenna, and Dr. D. L. Plazek for useful discussions. This work was supported by Advanced Acoustic Concepts of Columbia, MD and the Office of Naval Research.

- <sup>1</sup>J. D. Ferry, *Viscoelastic Properties of Polymers*, 3rd ed. (Wiley, New York, 1980), Chap. 11.
- <sup>2</sup>W. Philippoff and J. Brodnyan, "Preliminary results in measuring dynamic compressibilities," *J. Appl. Phys.* **26**, 846–849 (1955).
- <sup>3</sup>J. E. McKinney, S. Edelman, and R. S. Marvin, "Apparatus for the direct determination of the dynamic bulk modulus," *J. Appl. Phys.* **27**, 425–430 (1956).
- <sup>4</sup>J. E. McKinney, H. V. Belcher, and R. S. Marvin, "The dynamic compressibility of a rubber-sulfur vulcanizate and its relation to free volume," *Trans. Soc. Rheol.* **4**, 347–362 (1960).
- <sup>5</sup>J. Burns, P. S. Dubbelday, and R. Y. Ting, "Dynamic bulk modulus of various elastomers," *J. Polym. Sci., Part B: Polym. Phys.* **28**, 1187–1205 (1990).
- <sup>6</sup>P. S. Dubbelday and J. Burns, "Dynamic bulk modulus of soft elastomers," *J. Wave-Material Interaction* **5** and **6**, 181–210 (1991).
- <sup>7</sup>B. P. Holownia and E. H. James, "Determination of dynamic bulk modu-

lus of elastomers using pressure measurement," *Rubber Chem. Technol.* **66**, 749–753 (1993).

- <sup>8</sup>R. L. Willis, T. S. Stone, Y. H. Bertholot, and W. M. Madigosky, "An experimental-numerical technique for evaluating the bulk and shear dynamic moduli of viscoelastic materials," *J. Acoust. Soc. Am.* **102**, 3549–3555 (1997).
- <sup>9</sup>R. L. Willis, L. Wu, and Y. H. Bertholot, "Determination of the complex Young and shear dynamic moduli of viscoelastic materials," *J. Acoust. Soc. Am.* **109**, 611–621 (2001).
- <sup>10</sup>R. Meister, C. J. Marhoefer, R. Sciamanda, L. Cotter, and T. Litovitz, "Ultrasonic viscoelastic properties of associated liquids," *J. Appl. Phys.* **31**, 854–870 (1960).
- <sup>11</sup>A. DiMeglio and L. S. Wang, "A variational method for the identification of viscoelastic parameters from experimental data," *J. Acoust. Soc. Am.* **108**, 2746–2753 (2000).
- <sup>12</sup>J. C. Piquette, "Determination of the complex dynamic bulk modulus of elastomers by inverse scattering," *J. Acoust. Soc. Am.* **77**, 1665–1673 (1985).
- <sup>13</sup>M. P. Hagelberg and R. D. Corsaro, "A small pressurized vessel for measuring the acoustic properties of materials," *J. Acoust. Soc. Am.* **77**, 1222–1228 (1985).
- <sup>14</sup>I. D. Groves, "Twenty years of underwater electroacoustic standards," Naval Research Laboratory Formal Report, No. FR-07735 (1975).
- <sup>15</sup>K. W. Ng, "Transducer structure," US Patent 5,367,500, issued 22 November 1994.
- <sup>16</sup>H. Wang, Q. M. Zhang, L. E. Cross, and A. O. Sykes, "Clamping effect on the piezoelectric properties of poly(vinylidene fluoride-trifluoroethylene) copolymer," *Ferroelectrics* **150**, 255–266 (1993).
- <sup>17</sup>S. F. Morse, P. L. Marston, and G. Kaduchak, "High-frequency back-scattering enhancements by thick finite cylindrical shells in water at oblique incidence," *J. Acoust. Soc. Am.* **103**, 785–794 (1998).
- <sup>18</sup>A. J. Rudgers and C. A. Solvoid, "Apparatus-independent acoustical-material characteristics obtained from panel-test measurements," *J. Acoust. Soc. Am.* **76**, 926–934 (1984).
- <sup>19</sup>J. C. Piquette, "Direct measurements of edge diffraction from soft underwater acoustic panels," *J. Acoust. Soc. Am.* **95**, 3090–3099 (1994).
- <sup>20</sup>J. C. Piquette, "Conventional oblique-incidence panel test procedures," Naval Undersea Warfare Center-NPT Technical Memorandum 01-035 (2001).
- <sup>21</sup>J. A. Archer-Hall and D. Gee, "A single integral computer method for axisymmetric transducers with various boundary conditions," *NDT Int.* **13**, 95–101 (1980).
- <sup>22</sup>N. Yen, private communication.
- <sup>23</sup>L. E. Kinsler, A. R. Frey, A. B. Coppens, and J. V. Sanders, *Fundamentals of Acoustics*, 3rd ed. (Wiley, New York, 1982), p. 107, Eq. 5.22.
- <sup>24</sup>R. Kronig, "On the theory of dispersion of x-rays," *J. Opt. Soc. Am.* **12**, 547–557 (1926).
- <sup>25</sup>R. Kronig and H. A. Kramers, "Zur theorie der absorption und dispersion in den Röntgenspektren (Theory of absorption and dispersion in x-ray spectra)," *Z. Phys.* **48**, 174–179 (1928).
- <sup>26</sup>M. O'Donnell, E. T. Jaynes, and J. G. Miller, "Kramers–Kronig relationship between ultrasonic attenuation and phase velocity," *J. Acoust. Soc. Am.* **69**, 696–701 (1981).
- <sup>27</sup>P. G. Santangelo and C. M. Roland, "Temperature dependence of mechanical and dielectric relaxation in *cis*-1,4-polyisoprene," *Macromolecules* **31**, 3715–3719 (1998).
- <sup>28</sup>D. J. Plazek, "Temperature dependence of viscoelastic behavior of polystyrene," *J. Phys. Chem.* **69**, 3480–3487 (1965).
- <sup>29</sup>D. J. Plazek, "Temperature-dependence of the viscoelastic behavior of poly(vinyl acetate)," *Polymer J.* **12**, 43–53 (1980).
- <sup>30</sup>K. L. Ngai, A. Schonhals, and E. Schlosser, "An explanation of anomalous dielectric-relaxation properties of poly(propylene glycol)," *Macromolecules* **25**, 4915–4919 (1992).
- <sup>31</sup>D. J. Plazek, C. Bero, S. Neumeister, G. Floudas, G. Fytas, and K. L. Ngai, "Viscoelastic properties of amorphous polymers. 3. Low-molecular-weight poly(methylphenylsiloxane)," *Colloid Polym. Sci.* **272**, 1430–1438 (1994).
- <sup>32</sup>L. I. Palade, V. Verney, and P. Attane, "Time-temperature superposition and linear viscoelasticity of polybutadienes," *Macromolecules* **28**, 7051–7057 (1995).
- <sup>33</sup>D. J. Plazek, I.-C. Chay, K. L. Ngai, and C. M. Roland, "Viscoelastic properties of polymers. 4. Thermorheological complexity of the softening dispersion in polyisobutylene," *Macromolecules* **28**, 6432–6436 (1995).

- <sup>34</sup>D. J. Plazek and D. L. Plazek, "Viscoelastic behavior of atactic polypropylene," *Macromolecules* **16**, 1469–1475 (1983).
- <sup>35</sup>P. G. Santangelo, K. L. Ngai, and C. M. Roland, "Temperature dependence of relaxation in polypropylene and poly(ethylene-co-propylene)," *Macromolecules* **29**, 3651–3653 (1996).
- <sup>36</sup>M. L. Williams, R. F. Landel, and J. D. Ferry, "Mechanical properties of substances of high molecular weight. 19. The temperature dependence of relaxation mechanisms in amorphous polymers and other glass-forming liquids," *J. Am. Chem. Soc.* **77**, 3701–3707 (1955).
- <sup>37</sup>R. N. Capps, "Dynamic Young's moduli of some commercially available polyurethanes," *J. Acoust. Soc. Am.* **73**, 2000–2005 (1983).
- <sup>38</sup>J. Jarzynski, "Mechanisms of Sound Attenuation in Materials," in *Sound and Vibration Damping with Polymers*, edited by R. D. Corsaro and L. H. Sperling, ACS Symposium Series 424 (American Chemical Society, Washington, DC, 1990).
- <sup>39</sup>C. A. Bero and D. J. Plazek, "Volume-dependent rate-processes in an epoxy-resin," *J. Polym. Sci., Part B: Polym. Phys.* **29**, 39–47 (1991).
- <sup>40</sup>C. G. Robertson, J. E. Monat, and G. L. Wilkes, "Physical aging of an amorphous polyimide: enthalpy relaxation and mechanical property changes," *J. Polym. Sci., Part B: Polym. Phys.* **37**, 1931–1946 (1999).
- <sup>41</sup>S. L. Simon, J. W. Sobieski, and D. J. Plazek, "Volume and enthalpy recovery of polystyrene," *Polymer* **42**, 2555–2567 (2001).
- <sup>42</sup>G. B. McKenna, Y. Leterrier, and C. R. Schultheisz, "The evolution of material properties during physical aging," *Polym. Eng. Sci.* **35**, 403–410 (1995).
- <sup>43</sup>M. M. Santore, R. S. Duran, and G. B. McKenna, "Volume recovery in epoxy glasses subjected to torsional deformations—the question of rejuvenation," *Polymer* **32**, 2377–2381 (1991).